Magnetic order in nanoscale gyroid networks

Ami S. Koshikawa [1,2] Justin Llandro [3,4] Masayuki Ohzeki,[1,2,5] Shunsuke Fukami [3,4,6,7,8]
Hideo Ohno [3,4,6,7] and Naëmi Leo [9,10,*]
[1] *Graduate School of Information Sciences, Tohoku University, Sendai 980-8579, Japan*
[2] *Sigma-i Co. Ltd., Minato-ku, Tokyo 108-0075, Japan*
[3] *Research Institute of Electrical Communication, Tohoku University, Sendai 980-8577, Japan*
[4] *Center for Science and Innovation in Spintronics, Tohoku University, Sendai 980-8577, Japan*
[5] *International Research Frontiers Initiative, Tokyo Institute of Technology, Shibaura, Minato-ku, Tokyo 108-0023, Japan*
[6] *Center for Innovative Integrated Electronic Systems, Tohoku University, Sendai 980-0845, Japan*
[7] *WPI Advanced Institute for Materials Research, Tohoku University, Sendai 980-8577, Japan*
[8] *Inamori Research Insitute for Science, Kyoto 600-8411, Japan*
[9] *Instituto de Nanociencia y Materiales de Aragón, CSIC–Universidad de Zaragoza, 50009 Zaragoza, Spain*
[10] *CIC nanoGUNE BRTA, 20018 Donostia–San Sebastián, Spain*

(Received 10 March 2023; revised 21 June 2023; accepted 22 June 2023; published xxxxxxxxxx)

Three-dimensional magnetic metamaterials feature interesting phenomena that arise from a delicate interplay of material properties, local anisotropy, curvature, and connectivity. A particularly interesting magnetic lattice that combines these aspects is that of nanoscale gyroids, with a highly interconnected chiral network with local three-connectivity reminiscent of three-dimensional artificial spin ices. Here, we use finite-element micromagnetic simulations to elucidate the anisotropic behavior of nanoscale nickel gyroid networks at applied fields and at remanence. We simplify the description of the micromagnetic spin states with a macrospin model to explain the anisotropic global response, to quantify the extent of icelike correlations, and to discuss qualitative features of the anisotropic magnetoresistance in the three-dimensional network. Our results demonstrate the large variability of the magnetic order in extended gyroid networks, which might enable future spintronic functionalities, including neuromorphic computing and nonreciprocal transport.

DOI: 10.1103/PhysRevB.00.004400

I. INTRODUCTION

Networks of interacting nanomagnetic wires offer insight into emergent phenomena and functionalities arising from the underlying geometrical design and local connectivity. A well-studied class of these networks is two-dimensional artificial spin ices and magnonic crystals [1–3], which allow observations via imaging or magnetotransport of icelike low-energy states [4–6] and monopolelike excitations [7–9]. Because of the stochastic behavior and large reconfigurability of interacting interconnected lattices, such magnetic metamaterials have also been proposed for neuromorphic-inspired unconventional computational tasks [10–12].

Extending the study of emergent magnetic phenomena from planar two-dimensional to three-dimensional lattices promises novel functionalities [13–16], related to magnetochiral effects in curvilinear geometries [17–19], fast magnetization dynamics [20–23], and network topologies with dense connections to distant neighbors [24–26]. Notable examples of magnetic three-dimensional networks studied so far include inverse opals [27–30], magnetic buckyballs [21,31], and single-diamond lattices [20,24]. In these studies, the connecting struts are usually several hundred nanometers long and thus much larger than typical magnetic length scales, weakening possible curvilinear magnetic effects expected in truly nanoscale three-dimensional (3D) networks.

Gyroid structures grown by polymer self-assembly feature a highly interconnected three-dimensional network, a global chiral structure, and a lattice periodicity on the order of a few tens of nanometers. Recent studies on photonic gyroids demonstrated selective reflection of circularly polarized light [32] and the emergence of Weyl points [33–35]. With respect to magnetism, the local curvature of the gyroid is large enough to support a sizable geometrical Dzyaloshinskii-Moriya interaction [17,18], and its inherent chirality can give rise to emergent nonreciprocal effects [36–38], such as electrical magnetochiral anisotropy [39,40]. In our previous work [41], we imaged the magnetic states of nanoscale gyroids using electron holography and observed complex magnetic states. However, the local spin anisotropy has not been elucidated, and therefore, possible icelike correlations in magnetic gyroids have not yet been quantified so far.

Here, we use finite-element micromagnetic simulations to show that the field-driven and relaxed spin configurations of nanoscale nickel gyroids feature complex magnetic states arising from the nontrivial local anisotropy and the three-connectivity of the gyroid lattice, including the emergence of spin chiral effects. We discuss how the description of local spin order can be simplified using a macrospin model. We

*naemi.leo@unizar.es

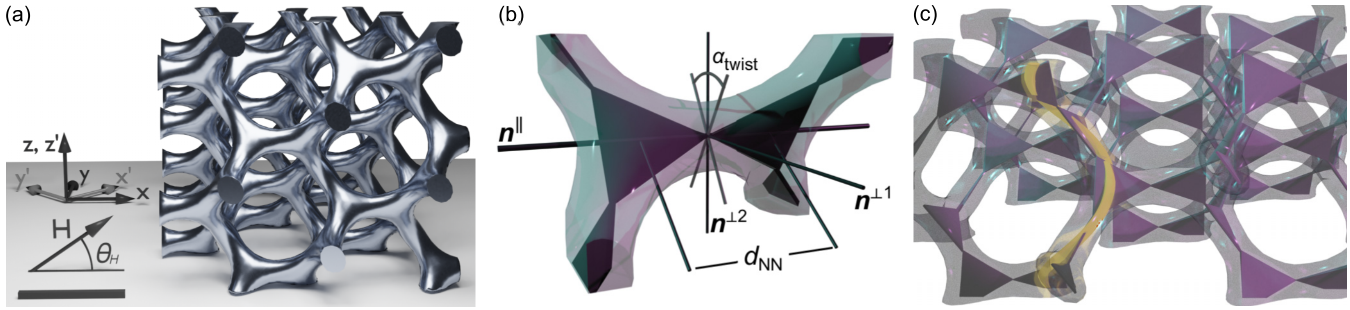

FIG. 1. Gyroid geometry. (a) Gyroid structure used for micromagnetic simulations, with directions of the cubic coordinate system (x', y', z') and simulation coordinates (x, y, z). A magnetic field was applied in the xz plane at angle θ_H to the x direction. The scale bar measures 50 nm. (b) Definition of the local coordinate axes $\hat{\mathbf{n}}_i^{\parallel}$, $\hat{\mathbf{n}}_i^{\perp 1}$, and $\hat{\mathbf{n}}_i^{\perp 2}$, with $\mathbf{n}_i^{\parallel}$ struts connecting neighboring vertices with distance d_{NN}. The planes of neighboring triangular plaquettes, with nodes centered on each strut, have a relative twist of $\alpha_{\mathrm{twist}} \approx 70.5^\circ$. (c) The gyroid can be represented by a highly connected network of corner-sharing triangular plaquettes. The yellow line highlights the tightest helix path used to calculate the maximum spin canting angle $\psi_{\mathrm{gDMI}}^{\max}$ due to the geometric Dzyaloshinskii-Moriya interaction.

furthermore illustrate how the anisotropic magnetoresistance in finite-size gyroid networks, which, due to the inherently noncoplanar spin configuration as well as the 3D network connectivity, shows behavior distinct from the response of bulk or planar devices. Our results underline the complexity of magnetic order in nanoscale 3D gyroids with inherently noncoplanar and frustrated spin order. These properties make gyroid networks ideal candidates for future studies of nonreciprocal effects or as a platform for probabilistic and neuromorphic computing schemes.

II. THE GYROID GEOMETRY

A single gyroid, like that shown in Fig. 1(a), derived from the Schoen G triply periodic minimal surface [42], is a 3D periodic network of connected struts which form chiral triple junctions. While gyroid photonic crystals are found in nature in the wings of some butterflies [43,44], nanoscale gyroids with lattice periodicities a in the range of 40 to 100 nm can be grown with large structural coherence over a few hundred micrometers by self-assembly of di- and triblock copolymer templates [45–47]. Selective etching followed by metal electrodeposition into the remaining scaffold results in single-gyroid network nanostructures with volume fill fractions f_V between 10% and 30% [48].

Many of the interesting physical phenomena in gyroids are related to its inherent chirality, described by the cubic-centered space group $I4_132$ (which allows for uniquely left- or right-handed gyroid structures), and the connectivity, mathematically also described as the *srs* net or K_4 crystal [49,50]. Vertices are connected to their neighbors by struts of length $d_{\mathrm{NN}} = a/\sqrt{8}$, with a being the cubic lattice constant. Each cubic unit cell contains eight individual vertices and 18 struts. For each of the six strut directions, a local coordinate system can be defined as shown in Fig. 1(b) and summarized in Table I, with $\hat{\mathbf{n}}_i^{\parallel}$ denoting the main strut direction and neighboring triangle planes rotated by $\alpha_{\mathrm{twist}} \approx 70.5^\circ$.

Due to its underlying three-connectivity, the gyroid network can also be represented by corner-sharing triangles, as shown in Fig. 1(c), reminiscent of geometrically frustrated magnetic systems that promote complex spin states, zero-temperature entropy, and other interesting emergent properties like magnetic monopoles [51–53]. Furthermore, a multitude of possible paths through the network exist. These include gyrating channels, such as the one highlighted yellow in Fig. 1(c) corresponding to the tightest possible helix path through the gyroid with radius $r_H = a/(4\sqrt{2})$ and periodicity $p_H = a$.

III. MICROMAGNETIC SIMULATIONS

Inspired by single-gyroid networks grown by self-assembly and studied by electron holography [41], in this work we focus on gyroids with a cubic lattice constant $a = 65$ nm and a volume fraction of $f_V = 17\%$. We use a coordinate system (x, y, z) rotated by 45° around the z' direction (with cubic crystallographic coordinates x', y', z'), as polymer gyroid templates yield preferential growth along the [110] direction.

We performed finite-element micromagnetic simulations to study the magnetic-field-driven response of a nickel gyroid structure, using the software FINMAG [54]. Magnetic properties of nickel were described by saturation magnetization $M_{\mathrm{sat}} = 485$ kA/m and an exchange constant $A_{\mathrm{ex}} = 8$ pJ/m. We assumed vanishing magnetocrystalline anisotropy, i.e., $K = 0$. The mesh of this gyroid simulation cell with a volume of $2\sqrt{2}a \times 2\sqrt{2}a \times 2a$, i.e., $184 \times 184 \times 130$ nm^3, as shown in Fig. 1(a), was generated using COMSOL MULTIPHYSICS [55]

TABLE I. Local coordinate systems for the six unique strut directions in the gyroid network, expressed with respect to coordinates x, y, and z of the simulation coordinate systems. The local normalized direction vectors $\hat{\mathbf{n}}_i^{\parallel}$, $\hat{\mathbf{n}}_i^{\perp 1}$, and $\hat{\mathbf{n}}_i^{\perp 2} = \mathbf{n}_i^{\parallel} \times \mathbf{n}_i^{\perp 1}$ form a right-handed system, in agreement with the overall right-handed chirality of our gyroid lattice.

Strut i	$\hat{\mathbf{n}}_i^{\parallel}$	$\hat{\mathbf{n}}_i^{\perp 1}$	$\hat{\mathbf{n}}_i^{\perp 2}$
1	$(+1, 0, 0)$	$(0, 0, -1)$	$(0, +1, 0)$
2	$(0, +1, 0)$	$(0, 0, -1)$	$(+1, 0, 0)$
3	$(+\frac{1}{2}, +\frac{1}{2}, +\frac{1}{\sqrt{2}})$	$(+\frac{1}{\sqrt{2}}, -\frac{1}{\sqrt{2}}, 0)$	$(+\frac{1}{2}, +\frac{1}{2}, -\frac{1}{\sqrt{2}})$
4	$(-\frac{1}{2}, -\frac{1}{2}, +\frac{1}{\sqrt{2}})$	$(+\frac{1}{\sqrt{2}}, -\frac{1}{\sqrt{2}}, 0)$	$(+\frac{1}{2}, +\frac{1}{2}, +\frac{1}{\sqrt{2}})$
5	$(+\frac{1}{2}, -\frac{1}{2}, +\frac{1}{\sqrt{2}})$	$(-\frac{1}{\sqrt{2}}, -\frac{1}{\sqrt{2}}, 0)$	$(+\frac{1}{2}, -\frac{1}{2}, -\frac{1}{\sqrt{2}})$
6	$(-\frac{1}{2}, +\frac{1}{2}, +\frac{1}{\sqrt{2}})$	$(+\frac{1}{\sqrt{2}}, +\frac{1}{\sqrt{2}}, 0)$	$(+\frac{1}{2}, -\frac{1}{2}, +\frac{1}{\sqrt{2}})$

and contained 18 196 nodes with a mean edge distance of 4.4 nm (i.e., smaller than the magnetostatic exchange length $l_{ex} = \sqrt{2A_{ex}\,\mu_0^{-1}M_{sat}^{-2}} = 7.5\,\text{nm}$).

For applied magnetic fields $H(\sin\theta_H, 0, \cos\theta_H)$, equivalent to in-plane fields for gyroid films grown by self-assembly, and a randomized initial spin configuration, micromagnetic configurations $\mathbf{m}(\mathbf{r})$ were obtained after relaxation. The external field was then switched off, $H = 0$, and the spin configuration was again relaxed to obtain states at remanence. This process was repeated for angles θ_H between 0° and 360° in 15° increments and at field magnitudes $H = 1\,\text{T}$, 100 mT, and 20 mT.

Analysis of the collective response was performed using the PYTHON package NETWORKX [56] by associating the local macrospins $\mathbf{s}_i$ of the gyroid structure with the edges of the underlying *srs* network. This allowed us to calculate properties such as the scalar spin chirality Ω_s, local ice rules A_{ice}, and the anisotropic magnetoresistance as the network resistance between specified nodes.

IV. RESULTS AND DISCUSSION

In the following, we will first discuss the global field-driven response of a single-gyroid structure, then assess the local anisotropy of the individual struts to justify a macrospin picture of the gyroid network. We then turn to collective properties such as the magnetic order emerging on triangular plaquettes and the global response from current transport through the network.

A. Global response

From the field- and field-angle-dependent micromagnetic simulation, we obtain the magnetization profile $\mathbf{m}(\mathbf{r})$ of the gyroid structure. Figure 2 shows the relation between the field angle θ_H in the xz plane (with $\theta_H = 0$ for $\mathbf{H} \parallel x$) and both the average magnetization magnitude $|M|$ and direction $\theta_M(\theta_H)$, defined by

$$\tan(\theta_H) = \frac{H_z}{H_x}, \tag{1}$$

$$\tan[\theta_M(\theta_H)] = \frac{\langle \mathbf{m}(\mathbf{r}, \theta_H)\rangle_z}{\langle \mathbf{m}(\mathbf{r}, \theta_H)\rangle_x}. \tag{2}$$

At high magnetic fields of 1 T (solid gray line and gray squares) the sample magnetization follows that of the applied field, i.e., $\theta_M = \theta_H$, indicating that the structure is saturated. In contrast, at fields of 100 mT the sample shows a slightly nonisotropic response [dashed blue line in Fig. 2(a)]. Configurations relaxed from 100 mT (dashed red line and red circles) and 1 T (not shown) are qualitatively similar. They feature a reduced net moment, and the magnetization direction θ_M exhibits four distinct plateaus. The steplike reorientations occur around angles $0^\circ \pm \alpha_s$ and $180^\circ \pm \alpha_s$, marked by vertical dashed lines in Fig. 2, with angles $\alpha_s = \tan^{-1}(\sqrt{1/2}) \approx 35.4^\circ$ in the xy plane perpendicular to some of the struts. The anisotropic global response and prominent demagnetization therefore indicate that the gyroid network plays a major role in the hysteretic behavior.

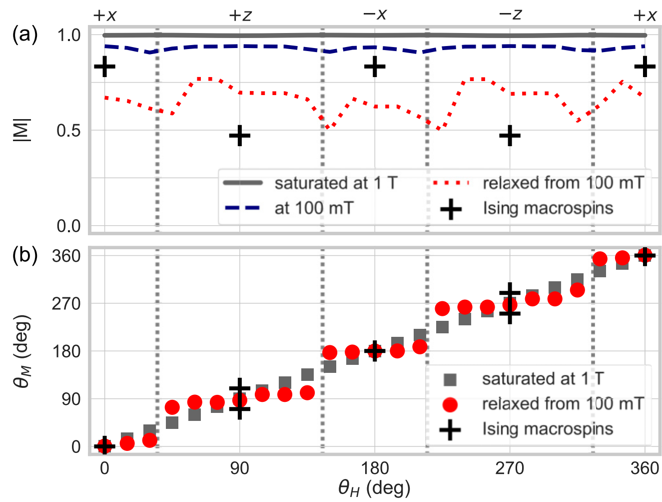

FIG. 2. Global anisotropic response. (a) Net magnetization $|M|$ of the gyroid dependent on the field angle θ_H. (b) Angle of the mean magnetization θ_M versus the field direction θ_H. At high fields (1 T, gray line and gray dots) the magnetization direction follows the field, i.e., $\theta_M = \theta_H$ and $M(\theta_H) \approx 1$. In the remanent state relaxed from high fields (from 100 mT, shown by a red dotted line and red squares) the magnetization direction shows four distinct plateaus, indicating preferential switching at angles related to the orientation of specific struts (vertical dotted lines).

The response at 20 mT and the obtained remanent state indicate unsystematic minor magnetic loops and thus are excluded from the following discussion.

B. Testing the macrospin assumption

The simplest model to describe the magnetic order of a gyroid network would be an Ising system: As shown in Fig. 2(a), the idea is to average the moments in each strut to a macrospin $\mathbf{s}_i$, and the shape anisotropy forces this macrospin to be parallel to the local strut direction $\hat{\mathbf{n}}_i^{\parallel}$. With this Ising macrospin assumption, values of $|M|$ and θ_M at remanence can be predicted at specific field angles θ_H by averaging over the six strut directions (Table I), as shown by black crosses in Fig. 2. For the moment direction θ_M in Fig. 2(b), the Ising macrospin picture yields $\theta_M = 0^\circ$ at $\theta_H = 0^\circ$ and $\theta_M = \alpha_{\text{twist}}$ or $\theta_M = 180^\circ - \alpha_{\text{twist}}$ at $\theta_H = 90^\circ$, in reasonably good agreement with the micromagnetic simulation results.

The reasonable similarity between global and Ising-like behaviors justifies a closer look at the local anisotropies of the strut magnetization: We obtain the magnitude and direction of strut macrospins $\mathbf{s}_i$ as the average of the local moment $\mathbf{m}(\mathbf{r})$ within nonoverlapping spherical volumes centered on each strut position $\mathbf{r}_i^{\text{cen}}$, as shown in Fig. 3(a):

$$\mathbf{s}_i = \sum_{|\mathbf{r}-\mathbf{r}_i^{\text{cen}}| \leqslant r_s} \mathbf{m}(\mathbf{r}). \tag{3}$$

With radius $r_s = \frac{2}{5} d_{\text{NN}} = a/(5\sqrt{2})$ the integration volumes contain about 67 ± 11 mesh points. Using this approach, we simplify the full micromagnetic configuration with 18 196 mesh nodes to 192 individual struts. We furthermore discard struts at the boundary of the simulation volume and in the

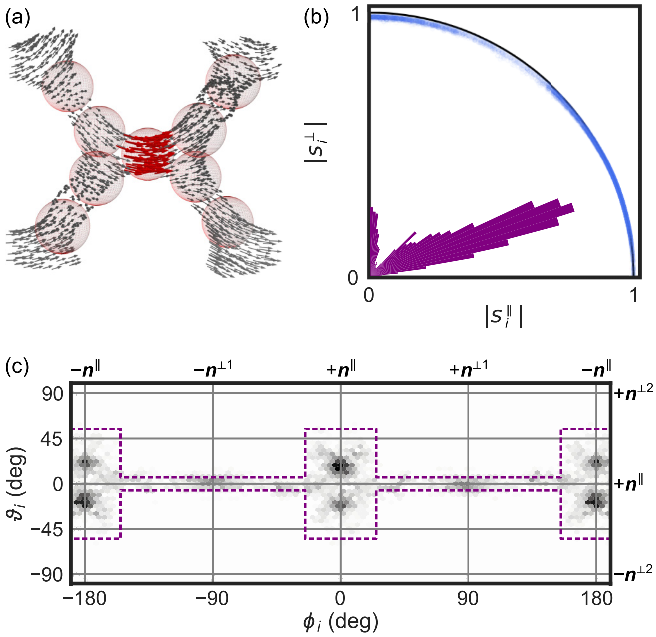

FIG. 3. Macrospin assumption. (a) The macrospin $\mathbf{s}_i$ is defined as the mean moment within nonoverlapping volumes centered on each strut (red spheres). (b) The magnitude of each strut moment $|\mathbf{s}_i| = |\mathbf{s}_i^{\parallel} + \mathbf{s}_i^{\perp}|$ at remanence (blue points) is close to 1 (black line), indicating that each strut acts as a macrospin. The rose diagram indicates non-Ising-like behavior with a median inclination of about 25° from the local direction $\hat{\mathbf{n}}_i^{\parallel}$. (c) Moment orientation of the macrospins at remanence, described by spherical angles ϕ_i and ϑ_i in the local coordinate system, showing signatures of chiral magnetic order. In 90% of the cases, the local moment lies within the region outlined in purple.

following consider the properties of 160 struts for each field magnitude and angle.

As shown in Fig. 3(b), at remanence the strut moments do, indeed, behave like macrospins, albeit not with the expected Ising-like anisotropy: Here, we separate each strut moment into parallel and perpendicular components with respect to the local main strut direction $\hat{\mathbf{n}}_i^{\parallel}$, $\mathbf{s}_i = \mathbf{s}_i^{\parallel} + \mathbf{s}_i^{\perp}$. Using this decomposition, in Fig. 3(b) we see that the net amplitude $|\mathbf{s}_i|$ (blue dots) is close to 1 (black line), indicating a locally saturated magnetization, with a reduction of at most 3%. Therefore, we can conclude that the macrospin assumption holds well, which is not entirely surprising: Each strut has a volume corresponding to a cylinder with a 10 nm diameter and 25 nm length, dimensions which are comparable to the exchange length $l_{\text{ex}} = 7.5$ nm and thus support quasiuniform strut magnetization without the formation of domain walls.

C. Local magnetic anisotropy

Even though the struts' behavior can be approximated with quasiuniform macrospins, the local anisotropy does not favor simple Ising-like behavior. This is illustrated by the rose diagram in Fig. 3(b) (purple bars), which indicates that the macrospins $\mathbf{s}_i$ have a median inclination of about 25° to the main strut axis $\hat{\mathbf{n}}_i^{\parallel}$. Further insight into the local anisotropy can be gained by considering the spherical angles ϕ_i and ϑ_i, which denote the macrospin orientation with respect to the local coordinate system defined in Table I:

$$\tan(\phi_i) = \frac{\mathbf{s}_i \cdot \hat{\mathbf{n}}_i^{\perp 1}}{\mathbf{s}_i \cdot \hat{\mathbf{n}}_i^{\parallel}}, \tag{4}$$

$$\tan(\vartheta_i) = \frac{\mathbf{s}_i \cdot \hat{\mathbf{n}}_i^{\perp 2}}{\sqrt{(\mathbf{s}_i \cdot \hat{\mathbf{n}}_i^{\parallel})^2 + \left(\mathbf{s}_i \cdot \hat{\mathbf{n}}_i^{\perp 1}\right)^2}}. \tag{5}$$

As shown in Fig. 3(c), 90% of the moments fall into the area outlined by the dashed purple line. This permissible angular range, describing preferential anisotropy, combines "wings" centered at $\phi_i = 0°$ and 180° with $\Delta\phi_i \approx \pm 25°$ and $\Delta\vartheta_i = \pm(90° - \alpha_s)$ with a "ring" in the $\hat{\mathbf{n}}_i^{\parallel}$–$\hat{\mathbf{n}}_i^{\perp 1}$ plane ($\phi_i = -180°$–$+180°$, $\Delta\vartheta_i = \pm\psi_{\text{gDMI}}$). Here, the angle $\psi_{\text{gDMI}}^{\max} = 6.5°$ is the maximum spin canting due to geometrical Dzyaloshinskii-Moriya interaction (gDMI) [18] predicted for the tightest possible helix path [yellow line in Fig. 1(c)].

The peculiar non-Ising, non-Heisenberg anisotropy is a direct consequence of at least three effects: (1) The wings in the anisotropy directly originate from the connectedness between vertices and the dominant exchange interaction which enforces magnetic continuity. As shown in Fig. 1(b), neighboring triangular plaquettes are noncoplanar; therefore, tilting of the moment away from $\hat{\mathbf{n}}_i^{\parallel}$ can be energetically favorable for minimizing the dipolar interactions between the net moments of the two vertices. However, tilting towards $\hat{\mathbf{n}}_i^{\perp 2}$ by more than $\pm(90° - \alpha_s)$ leads to energy-costly magnetic charges. (2) The ring corresponds to small spin canting up to maximum values $\psi_{\text{gDMI}}^{\max}$ due to geometrical DMI, showing a small asymmetry for fields at $\theta_H = \pm 90°$. (3) Slight asymmetries in the average angles $\langle\vartheta_i\rangle$ of macrospins at 0° and ±180° indicate a chiral contribution to the magnetic anisotropy, likely related to the underlying chiral right-handed crystal structure.

D. Hysteretic behavior

Figure 4 gives further insight to the relationship between local anisotropy and hysteretic behavior, broken down for individual struts i: Here, the local macrospin moments are indicated by black points, projected onto the corresponding coordinate system $\hat{\mathbf{n}}_i^{\parallel}$, $\hat{\mathbf{n}}_i^{\perp 1}$, and $\hat{\mathbf{n}}_i^{\perp 2}$. Colored arrows indicate the mean moment direction at a given field angle θ_H, averaged over all equivalent struts.

Figure 4(a) shows the behavior at applied fields of 0.1 T. As the field angle θ_H is defined in the global xz plane, the struts are differently oriented with respect to the simulation coordinate frame. Therefore, the same field pulls the strut moments in significantly different directions with respect to the local coordinate system. A field magnitude of 100 mT does not yet fully saturate the gyroid magnetization, and the effect of local anisotropy is evident from the nonuniform rotation of the moment with the field direction.

Figure 4(b) shows the equivalent moment configurations at remanence relaxed from 100 mT. The high-field state clearly influences the final configuration, and generally, four specific low-energy moment configurations can be classified for each strut, in accordance with the four plateaus of the global magnetization direction shown in Fig. 2 (red circles). The complex response of the local macrospins in combination

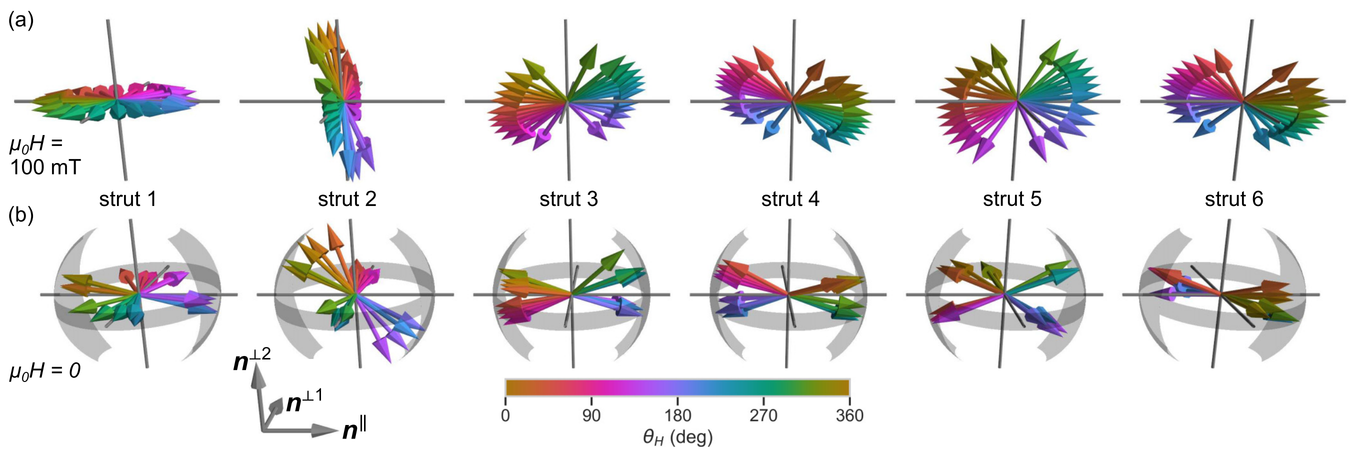

FIG. 4. Local hysteretic behavior, with the strut moments in the local coordinate system $\hat{\mathbf{n}}_i^{\parallel}$, $\hat{\mathbf{n}}_i^{\perp 1}$, and $\hat{\mathbf{n}}_i^{\perp 2}$ at (a) 100 mT and (b) at remanence relaxed from 100 mT. The colored arrows denote the mean magnetization corresponding to a specific field direction θ_H (color bar). (a) At 100 mT, the moment mainly follows the direction of the applied field. (b) At remanence, for each strut i the mean moment relaxes from the initial field direction θ_H into four angular quadrants, related to the four plateaus seen in the global response in Fig. 2(b).

with the highly connected network therefore leads to emergent collective order in extended gyroid networks.

E. Spin ice rules

To discuss possible collective effects in the gyroid network, we first focus on the statistical properties and magnetic connectivity of the corner-sharing triangular plaquettes, as shown in Fig. 1(c). In many cases, the spin order of frustrated magnetic networks with triangular plaquettes is governed by *local* ice rules instead of long-range *global* order [4–6,52,53]. To discuss the concept of ice rules in the gyroid network, in the following we consider the scalar Ising-like component of the strut macrospin s_i^I, defined by

$$s_i^I = \frac{\mathbf{s}_i \cdot \mathbf{r}^{\parallel,\mathrm{in}}}{|\mathbf{r}^{\parallel,\mathrm{in}}|}, \quad \mathbf{r}^{\parallel,\mathrm{in}} = \mathbf{r}_i - \langle \mathbf{r} \rangle_{1,2,3}. \tag{6}$$

Here, $\langle \mathbf{r} \rangle_{1,2,3}$ denotes the center of the corresponding triangular plaquette, as the mean value of coordinates from struts 1, 2, and 3. Thus, for Ising-like macrospins the values of s_i^I will be $+1$ (-1) for moments pointing into (out of) the center of the corresponding plaquette.

First, to test for icelike correlations we consider the scalar spin chirality [57,58] of each vertex as

$$\Omega_s = \tfrac{1}{3}\left(s_1^I s_2^I + s_2^I s_3^I + s_3^I s_1^I\right). \tag{7}$$

The scalar spin chirality Ω_s can take two limiting values: $\Omega_s = +1$, corresponding to all-in or all-out moment configurations, and $\Omega_s = -1/3$, which quantifies local icelike two-in-one-out (or vice versa) configurations. We found no single case corresponding to an all-in or all-out moment configuration, as such monopolelike configurations are too energetically costly to occur in our exchange-dominated nanoscale magnetic gyroid structure. At remanence, the median value for the spin chirality is $\langle \Omega_s \rangle = -0.29$, i.e., close to the theoretical value of $-1/3$, independent of the initial field direction θ_H. This finding indicates that the local magnetic order in gyroid networks is governed by spin ice rules.

To further quantify the local magnetic order, we now calculate the sum of the Ising-like moments of each triangular plaquette combining struts 1, 2, and 3:

$$A_{\mathrm{ice}} = s_1^I + s_2^I + s_3^I. \tag{8}$$

The quantity A_{ice} allows us to easily distinguish between two-in-one-out ($A_{\mathrm{ice}} = +1$) and one-in-two-out ($A_{\mathrm{ice}} = -1$) moment configurations. Since the local moments do not strictly follow the in-or-out Ising anisotropy, i.e., $|s_i^I| \leqslant 1$, values of A_{ice} between these two limits are also allowed. In particular, we find that values of A_{ice} around zero are highly likely, corresponding to triangular plaquettes in which one moment is approximately parallel to the one-in-one-out magnetization of the two opposite struts [Fig. 5(a)]. Because of the twist between neighboring plaquettes, this non-Ising moment will also be *noncoplanar* with respect to at least one triangle plane, which enables nonzero vector chirality terms [58] related to additional magnetic properties, such as nonreciprocal magnetotransport and spin-wave propagation [36–38].

Because of the dominant exchange interaction, the magnetic connection formed by a single strut is continuous; that is, a macrospin which points *out* of a triangular plaquette must point *into* the neighboring one. This continuity allows us to define a magnetic flux across the three-dimensional gyroid lattice (or *srs* net), where each triangle carries at least one one-in-one-out flux line or allows the bifurcation of two flux lines via two-in-one-out or one-in-two-out moment configurations.

Figure 5 illustrates the 3D connectivity of the magnetic flux at different fields and the corresponding remanent states. As shown in Fig. 5(a), the magnetic order is simplified by using triangular plaquettes colored by the value of A_{ice}. Neighboring corners i and j are connected by a black "flux" line if the pair corresponds to a one-in-one-out moment configuration, i.e., $s_i^I s_j^I < 0$, with the additional condition that the two moments are sufficiently Ising-like, i.e., $|s_{i,j}^I| \geqslant 0.5$. Under applied field [Figs. 5(b)–5(d)], the flux forms a regular pattern through the gyroid lattice, as the moments are largely aligned parallel

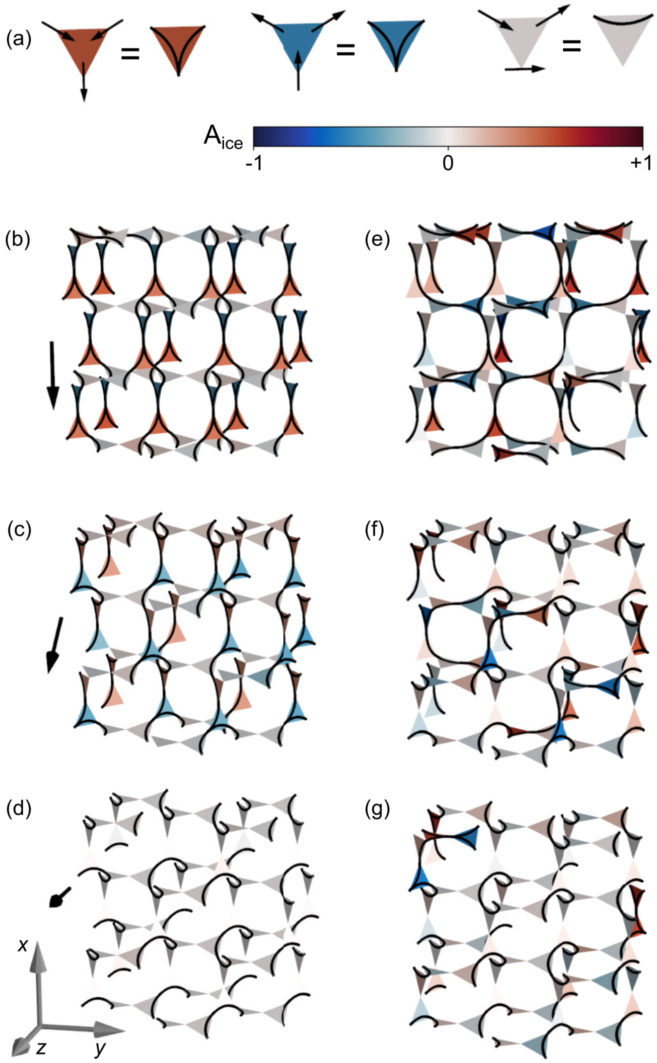

FIG. 5. Lattice flux in the gyroid network, which can be represented by (a) black lines that mark pairwise in-out macrospin configurations. The color scale for $A_{\rm ice}$ denotes two-in-one-out (red), one-in-two-out (blue), and one-in-one-out (gray) triangular plaquettes. Macrospin flux lattices formed by application of magnetic fields $|H| = 100\,$mT at angles (b) $\theta_H = 180^\circ$, (c) $\theta_H = 135^\circ$, and (d) $\theta_H = 90^\circ$ (see black arrow). (e)–(g) At remanence, relaxed from the respective configuration shown on the left, the overall magnetic connectivity and the 3D character of the flux lines through the gyroid lattice have increased.

to the field. Depending on the field direction θ_H, the flux distribution is mostly confined to the xz plane [Figs. 5(b) and 5(d) for $\theta_H = 180^\circ$ and 135°, respectively] or exhibits one-dimensional flux channels along z [Fig. 5(c), $\theta_H = 90^\circ$]. The magnetic configuration at remanence shown in Figs. 5(e)–5(g) has a higher connectivity and more plaquettes with an icelike two-in-two-out configuration compared to the high-field states they were relaxed from. This is especially the case for $\theta_H = 180^\circ$ [Fig. 5(e)], which features a complex three-dimensional flux network. Regardless of the increased magnetic connectivity, however, many triangular plaquettes still feature only one flux line due to a perpendicular moment on the third macrospin. Simulation results from minor loops (relaxed from 20 mT, not shown) resulted in a higher ratio of icelike correlations, indicating that a suitable demagnetization protocol could be used to relax the gyroid lattice to a low-energy configuration with predominant icelike correlations indicative of a highly frustrated spin system.

F. Magnetotransport

Finally, we consider the complex directional magnetotransport signatures emerging in the gyroid, which can be used to fingerprint the magnetic order and local anisotropy [36,37]. Because of the finite-size volume of the micromagnetic simulations, we here discuss the most salient features of only the anisotropic magnetoresistance (AMR), using a simplified geometrical model for magnetoresistance in networks [59].

For each strut in the gyroid lattice the AMR results in a variation of the local longitudinal resistance $\rho_i(\varphi_i)$ depending on the angle $\varphi_i = \sphericalangle(\mathbf{j}_i, \mathbf{s}_i)$ between the charge current flow direction $\mathbf{j}_i \parallel \hat{\mathbf{n}}_\parallel$ and the macrospin $\mathbf{s}_i$, with

$$\rho_i(\varphi_i) = \rho_0[1 + \Delta_{\rm AMR}\cos^2(\varphi_i)], \tag{9}$$

where ρ_0 and $\Delta_{\rm AMR}$ are the nonmagnetic resistance and the relative magnitude of the AMR effect of the underlying bulk material, respectively. For convenience, we set $\rho_0 = 1$. For nickel nanowires the typical AMR magnitude is on the order of $\Delta_{\rm AMR} = 1.5\%$ [60].

There are a multitude of possible paths connecting two chosen nodes A and B through the gyroid network, which act as parallel conduction channels with piecewise local resistances $\rho_i(\varphi_i)$. By applying Kirchhoff's law, one can calculate the effective network resistance $\rho_{A\to B}$, here using the function RESISTANCE_DISTANCE of the PYTHON package NETWORKX [56,61]. As the magnetic order is highly dependent on the field direction, we thus expect significant variation of $\rho^{\rm AMR}_{A\to B}(\theta_H)$ with both the field magnitude H and angle θ_H as well as the choice of A and B.

Figure 6 shows the AMR response for two node pairs A and B separated along the x direction [Figs. 6(a) and 6(b)] and along the z direction [Figs. 6(c) and 6(d)]. The top graphs illustrate parallel connections $A \to B$, highlighting the exponentially increasing number of possible paths with increasing path length. The bottom graphs show the angular dependence of the AMR calculated from the micromagnetic simulations, which originates from a mixture of the local magnetic anisotropy and the multitude of parallel paths through the network.

Before turning to the macrospin results, we briefly discuss three general limiting cases to the AMR within the gyroid network, indicated by dashed gray lines in Figs. 6(b) and 6(d): First, for the minimum nonmagnetic limit (AMR $=$ 0%, bottom line) the network resistance $\rho^{\rm NM}_{A\to B}$ is increased compared to the bulk value $\rho_0 = 1$ but significantly smaller than the length of the shortest paths $A \to B$ would imply, with $\rho^{\rm NM} = 2.68$ but $l_{\min} = 11d_{\rm NN}$ for Figs. 6(a) and 6(b) and $\rho^{\rm NM} = 2.18$ but $l_{\min} = 7d_{\rm NN}$ for Figs. 6(c) and 6(d). Second, the maximum limit for AMR (1.5%, top line) is achieved for perfect Ising-like macrospins, with $\mathbf{s}_i \parallel \hat{\mathbf{n}}_\parallel \parallel \mathbf{j}_i$. Third, for an infinite-size gyroid lattice the AMR response between nodes A and B is isotropic with respect to

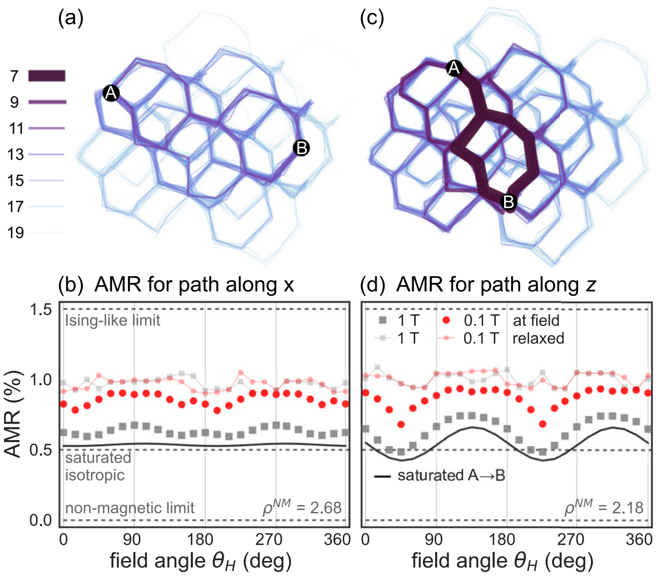

FIG. 6. Anisotropic magnetoresistance through a finite-size gyroid network. (a) Possible paths $A \rightarrow B$ connecting nodes A and B in the x direction, with different lengths indicated by line color and width. (b) Dependence of the relative AMR signal between nodes A and B on the field angle θ_H. Solid and dashed lines denote the limiting cases to the magnetoresistance in the gyroid network; squares and dots show the AMR signal calculated from the macrospin analysis of the micromagnetic simulations. ρ_{NM} denotes the nonmagnetic network resistance between A and B. (c) and (d) Equivalent observations for paths between A and B along the z direction, exhibiting more pronounced angular variation with θ_H.

θ_H; at $\mathrm{AMR}^{\mathrm{isotropic}}_{\mathrm{gyroid}} = \frac{1}{3}\max(\mathrm{AMR}_{\mathrm{bulk}})$, here, AMR $= 0.5\%$ (middle dashed line).

The field-saturated case highlights one stark difference between bulklike AMR and AMR in a gyroid network: In the bulk, the maximum AMR is observed at saturation with $\mathbf{M} \parallel \mathbf{H}$, whereas in the gyroid network, high fields destroy any Ising-like state that leads to maximum AMR. Instead, as shown by the black lines in Figs. 6(b) and 6(d), the field-saturated AMR, with $\mathbf{s}_i \parallel \mathbf{H}$ for each strut i along paths $A \rightarrow B$, lies in between the previously discussed limiting cases. The angular variation with θ_H is a direct consequence of the finite size and the relative importance of different strut directions within the connecting paths, as illustrated by the higher anisotropy in Fig. 6(d) compared to Fig. 6(b). This behavior means that measurements at saturation, rather than the magnetoresistance at remanence, are more likely to provide a reliable normalization in experimental studies of the magnetoresistive response of gyroid networks.

Somewhat surprisingly, the AMR at 1 T [gray squares in Figs. 6(b) and 6(d)] lies above the predicted saturated response (black line) and is also more anisotropic. This deviation is due to the fact that even though the net magnetization seems saturated [see Fig. 2(a)], the macrospins $\mathbf{s}_i$ can still have a slight inclination to the direction of $\mathbf{H}$ of about 3.5° to 5°. This value is consistent with the analytical predictions for spin canting induced by geometry-induced DMI ($\psi^{\max}_{\mathrm{gDMI}} = 6.5°$) discussed above.

As the field magnitude is decreased to 100 mT [red circles in Figs. 6(b) and 6(d)] the net AMR signal increases, and its angular variation is modified. This observation can be related to both the nonmonotonic rotation of the individual macrospins due to the intrinsic local anisotropy as represented in Fig. 4(a) and the collective response related to the emergent flux lattice shown in Fig. 5.

Finally, the AMR signal at remanence (lighter dots) lies about halfway between the limits of isotropic field saturation and the Ising-like limit, in agreement with the local non-Ising anisotropy. The angular variation of the remanent AMR is rather weak.

In conclusion, magnetoresistance signatures of gyroids give insight into the effective local magnetic anisotropy and emergent collective behavior. In comparison to two-dimensional (2D) artificial spin systems [4,9,59], there are notable differences in the magnetoresistive response of gyroids: First, there are many more possible conduction pathways, as wires can cross in 3D geometries but not in planar devices. Second, due to the regular 3D arrangement of struts, the spin order is inherently noncollinear *and* noncoplanar, irrespective of the direction and magnitude of any applied magnetic field. In combination with the high degree of frustration, magnetoresistance measurements including the anomalous Hall effect [4,9] and chiral magnetoresistance and nonreciprocal spin-wave propagation due to nonvanishing vector spin chirality [36,37,57] therefore could be the ideal tool to elucidate the emerging collective response of magnetic gyroids.

V. CONCLUSIONS AND OUTLOOK

In this work we considered the complex spin order of a gyroid network at applied magnetic fields and at remanence. Using micromagnetic simulations, we revealed that for nanoscale nickel gyroids the individual struts can be described as quasiuniform macrospins. Their complex configuration is affected by the three-dimensional network connectivity as well as modified by an effective chiral exchange term, the geometrical DMI. While the gyroid network is built from corner-sharing triangular plaquettes and thus is a prime host for geometrically frustrated spin order, the deviation from local Ising-like magnetic anisotropy reduces icelike correlations.

We find that magnetotransport signatures reflect the complexity of spin order within the gyroid lattice and are different from the magnetoresistive behavior of both bulk samples and 2D artificial spin systems. Especially in comparison to planar devices, the 3D geometry and connectivity, truly 3D spin order in response to 3D fields, and the multitude of parallel conduction channels of the regular gyroid network result in an extensive manifold of magnetic states and give many possible choices for magnetotransport geometries. This vast phase space therefore is ideal to explore for future three-dimensional spintronic applications [12,15].

For future experimental exploration of nanoscale gyroids prepared by different growth methods, such as polymer self-assembly [46–48], focused-electron beam induced deposition (FEBID) [62,63], and two-photon nanolithography [26,64,65], we identify two main aspects of emergent magnetic order to explore: First, our results indicate that highly frustrated spin configurations can be prepared with suitable demagnetization protocols in gyroid networks with enhanced Ising-like macrospin behavior (e.g., stabilized by the choice of materials or by preparing networks with larger lattice constants) and likely lead to interesting collective 3D artificial spin ice behavior. Second, due to their inherent noncoplanar spin order and thus nontrivial vector spin chirality, gyroid networks are ideal candidates to host directional magnetotransport and nonreciprocal spin wave propagation [36,37,57]. Such emergent properties and the intrinsic stochasticity related to frustrated magnetic order in nanoscale gyroids therefore makes them a rich platform to investigate 3D spintronic networks for probabilistic and neuromorphic computing [10–12,66].

ACKNOWLEDGMENTS

The authors thank A. Kakay and A. Fernández-Pacheco for helpful discussions. N.L. received funding from the European Research Council (ERC) under the European Union's Horizon 2020 research and innovation program under Marie Sklodowska Curie Grant Agreement No. 844304 (LICONAMCO), as well as support from the European Community under the Horizon 2020 program, Contract No. 101001290 (3DNANOMAG). The work of A.S.K. was financially supported by JSPS KAKENHI Grant No. 18J20396. The work of J.L. and S.F. was supported by JSPS KAKENHI Grants No. 21K04816 and No. 19H05622 and the Graduate Program for Spintronics (GP-Spin) as well as Cooperative Research Projects of RIEC, CSIS, and CSRN, Tohoku University.

[1] S. H. Skjærvø, C. H. Marrows, R. L. Stamps, and L. J. Heyderman, Advances in artificial spin ice, Nat. Rev. Phys. **2**, 13 (2019).

[2] S. Gliga, E. Iacocca, and O. G. Heinonen, Dynamics of reconfigurable artificial spin ice: Toward magnonic functional materials, APL Mater. **8**, 040911 (2020).

[3] A. Barman *et al.*, The 2021 magnonics roadmap, J. Phys.: Condens. Matter **33**, 413001 (2021).

[4] W. R. Branford, S. Ladak, D. E. Read, K. Zeissler, and L. F. Cohen, Emerging chirality in artificial spin ice, Science **335**, 1597 (2012).

[5] B. Canals, I.-A. Chioar, V.-D. Nguyen, M. Hehn, D. Lacour, F. Montaigne, A. Locatelli, T. O. Mentes, B. S. Burgos, and N. Rougemaille, Fragmentation of magnetism in artificial kagome dipolar spin ice, Nat. Commun. **7**, 11446 (2016).

[6] J. C. Gartside, D. M. Arroo, D. M. Burn, V. L. Bemmer, A. Moskalenko, L. F. Cohen, and W. R. Branford, Realization of ground state in artificial kagome spin ice via topological defect-driven magnetic writing, Nat. Nanotechnol. **13**, 53 (2018).

[7] E. Mengotti, L. J. Heyderman, A. F. Rodriguez, F. Nolting, R. V. Hugli, and H.-B. Braun, Real-space observation of emergent magnetic monopoles and associated Dirac strings in artificial kagome spin ice, Nature Phys. **7**, 68 (2011).

[8] N. Rougemaille, F. Montaigne, B. Canals, M. Hehn, H. Riahi, D. Lacour, and J.-C. Toussaint, Chiral nature of magnetic monopoles in artificial spin ice, New J. Phys. **15**, 035026 (2013).

[9] B. L. Le, J. Park, J. Sklenar, G.-W. Chern, C. Nisoli, J. D. Watts, M. Manno, D. W. Rench, N. Samarth, C. Leighton, and P. Schiffer, Understanding magnetotransport signatures in networks of connected permalloy nanowires, Phys. Rev. B **95**, 060405(R) (2017).

[10] R. W. Dawidek, T. J. Hayward, I. T. Vidamour, T. J. Broomhall, G. Venkat, M. A. Mamoori, A. Mullen, S. J. Kyle, P. W. Fry, N.-J. Steinke, J. F. K. Cooper, F. Maccherozzi, S. S. Dhesi, L. Aballe, M. Foerster, J. Prat, E. Vasilaki, M. O. A. Ellis, and D. A. Allwood, Dynamically-driven emergence in a nanomagnetic system, Adv. Funct. Mater. **31**, 2008389 (2021).

[11] J. C. Gartside, K. D. Stenning, A. Vanstone, H. H. Holder, D. M. Arroo, T. Dion, F. Caravelli, H. Kurebayashi, and W. R. Branford, Reconfigurable training and reservoir computing in an artificial spin-vortex ice via spin-wave fingerprinting, Nat. Nanotechnol. **17**, 460 (2022).

[12] D. Bhattacharya, Z. Chen, C. J. Jensen, C. Liu, E. C. Burks, D. A. Gilbert, X. Zhang, G. Yin, and K. Liu, 3D interconnected magnetic nanowire networks as potential integrated multistate memristors, Nano Lett. **22**, 10010 (2022).

[13] G.-W. Chern, C. Reichhardt, and C. Nisoli, Realizing three-dimensional artificial spin ice by stacking planar nano-arrays, Appl. Phys. Lett. **104**, 013101 (2014).

[14] Y. Perrin, B. Canals, and N. Rougemaille, Extensive degeneracy, coulomb phase and magnetic monopoles in artificial square ice, Nature (London) **540**, 410 (2016).

[15] A. Fernández-Pacheco, R. Streubel, O. Fruchart, R. Hertel, P. Fischer, and R. P. Cowburn, Three-dimensional nanomagnetism, Nat. Commun. **8**, 15756 (2017).

[16] D. Makarov, O. M. Volkov, A. Kákay, O. V. Pylypovskyi, B. Budinská, and O. V. Dobrovolskiy, New dimension in magnetism and superconductivity: 3D and curvilinear nanoarchitectures, Adv. Mater. **34**, 2101758 (2022).

[17] R. Streubel, P. Fischer, F. Kronast, V. P. Kravchuk, D. D. Sheka, Y. Gaididei, O. G. Schmidt, and D. Makarov, Magnetism in curved geometries, J. Phys. D **49**, 363001 (2016).

[18] O. M. Volkov, D. D. Sheka, Y. Gaididei, V. P. Kravchuk, U. K. Rößler, J. Fassbender, and D. Makarov, Mesoscale Dzyaloshinskii-Moriya interaction: Geometrical tailoring of the magnetochirality, Sci. Rep. **8**, 866 (2018).

[19] D. D. Sheka, O. V. Pylypovskyi, P. Landeros, Y. Gaididei, A. Kákay, and D. Makarov, Nonlocal chiral symmetry breaking in curvilinear magnetic shells, Commun. Phys. **3**, 128 (2020).

[20] S. Sahoo, A. May, A. van Den Berg, A. K. Mondal, S. Ladak, and A. Barman, Observation of coherent spin waves in a three-dimensional artificial spin ice structure, Nano Lett. **21**, 4629 (2021).

[21] R. Cheenikundil, J. Bauer, M. Goharyan, M. D'Aquino, and R. Hertel, High-frequency modes in a magnetic buckyball nanoarchitecture, APL Mater. **10**, 081106 (2022).

[22] L. Körber, R. Verba, J. A. Otálora, V. Kravchuk, J. Lindner, J. Fassbender, and A. Kákay, Curvilinear spin-wave dynamics

beyond the thin-shell approximation: Magnetic nanotubes as a case study, Phys. Rev. B **106**, 014405 (2022).
[23] L. Skoric, C. Donnelly, A. Hierro-Rodriguez, M. A. Cascales Sandoval, S. Ruiz-Gómez, M. Foerster, M. A. Niño, R. Belkhou, C. Abert, D. Suess, and A. Fernández-Pacheco, Domain wall automotion in three-dimensional magnetic helical interconnectors, ACS Nano **16**, 8860 (2022).
[24] A. May, M. Saccone, A. van den Berg, J. Askey, M. Hunt, and S. Ladak, Magnetic charge propagation upon a 3D artificial spin-ice, Nat. Commun. **12**, 3217 (2021).
[25] S. Koraltan, F. Slanovc, F. Bruckner, C. Nisoli, A. V. Chumak, O. V. Dobrovolskiy, C. Abert, and D. Suess, Tension-free Dirac strings and steered magnetic charges in 3D artificial spin ice, npj Comput. Mater. **7**, 125 (2021).
[26] P. Pip, S. Treves, J. R. Massey, S. Finizio, Z. Luo, A. Hrabec, V. Scagnoli, J. Raabe, L. Philippe, L. J. Heyderman, and C. Donnelly, X-ray imaging of the magnetic configuration of a three-dimensional artificial spin ice building block, APL Mater. **10**, 101101 (2022).
[27] N. A. Grigoryeva, A. A. Mistonov, K. S. Napolskii, N. A. Sapoletova, A. A. Eliseev, W. Bouwman, D. V. Byelov, A. V. Petukhov, D. Y. Chernyshov, H. Eckerlebe, A. V. Vasilieva, and S. V. Grigoriev, Magnetic topology of Co-based inverse opal-like structures, Phys. Rev. B **84**, 064405 (2011).
[28] I. S. Shishkin, A. A. Mistonov, I. S. Dubitskiy, N. A. Grigoryeva, D. Menzel, and S. V. Grigoriev, Nonlinear geometric scaling of coercivity in a three-dimensional nanoscale analog of spin ice, Phys. Rev. B **94**, 064424 (2016).
[29] A. A. Mistonov, I. S. Dubitskiy, I. S. Shishkin, N. A. Grigoryeva, A. Heinemann, N. A. Sapoletova, G. A. Valkovskiy, and S. V. Grigoriev, Magnetic structure of the inverse opal-like structures: Small angle neutron diffraction and micromagnetic simulations, J. Magn. Magn. Mater. **477**, 99 (2019).
[30] A. Rana, Jr. *et al.*, Three-dimensional topological magnetic monopoles and their interactions in a ferromagnetic metalattice, Nat. Nanotechnol. **18**, 227 (2023).
[31] R. Cheenikundil and R. Hertel, Switchable magnetic frustration in buckyball nanoarchitectures, Appl. Phys. Lett. **118**, 212403 (2021).
[32] M. D. Turner, M. Saba, Q. Zhang, B. P. Cumming, G. E. Schröder-Turk, and M. Gu, Miniature chiral beamsplitter based on gyroid photonic crystals, Nat. Photon. **7**, 801 (2013).
[33] M. Koshino and H. Aoki, Electronic structure of an electron on the gyroid surface: A helical labyrinth, Phys. Rev. B **71**, 073405 (2005).
[34] L. Lu, L. Fu, J. D. Joannopoulos, and M. Soljacic, Weyl points and line nodes in gyroid photonic crystals, Nat. Photon. **7**, 294 (2013).
[35] L. Lu, Z. Wang, D. Ye, L. Ran, L. Fu, J. D. Joannopoulos, and M. Soljačić, Experimental observation of Weyl points, Science **349**, 622 (2015).
[36] S. Seki, Y. Okamura, K. Kondou, K. Shibata, M. Kubota, R. Takagi, F. Kagawa, M. Kawasaki, G. Tatara, Y. Otani, and Y. Tokura, Magnetochiral nonreciprocity of volume spin wave propagation in chiral-lattice ferromagnets, Phys. Rev. B **93**, 235131 (2016).
[37] Y. Tokura and N. Nagaosa, Nonreciprocal responses from non-centrosymmetric quantum materials, Nat. Commun. **9**, 3740 (2018).
[38] A. Barman, S. Mondal, S. Sahoo, and A. De, Magnetization dynamics of nanoscale magnetic materials: A perspective, J. Appl. Phys. **128**, 170901 (2020).
[39] G. L. J. A. Rikken, J. Fölling, and P. Wyder, Electrical Magnetochiral Anisotropy, Phys. Rev. Lett. **87**, 236602 (2001).
[40] M. Atzori, C. Train, E. A. Hillard, N. Avarvari, and G. L. J. A. Rikken, Magneto-chiral anisotropy: From fundamentals to perspectives, Chirality **33**, 844 (2021).
[41] J. Llandro, D. M. Love, A. Kovács, J. Caron, K. N. Vyas, A. Kákay, R. Salikhov, K. Lenz, J. Fassbender, M. R. J. Scherer, C. Cimorra, U. Steiner, C. H. W. Barnes, R. E. Dunin-Borkowski, S. Fukami, and H. Ohno, Visualizing magnetic structure in 3D nanoscale Ni-Fe gyroid networks, Nano Lett. **20**, 3642 (2020).
[42] A. H. Schoen, *Infinite Periodic Minimal Surfaces without Self-Intersections* (NASA Electronics Research Center, Cambridge, MA, 1970).
[43] K. Michielsen and D. G. Stavenga, Gyroid cuticular structures in butterfly wing scales: Biological photonic crystals, J. R. Soc. Interface **5**, 85 (2008).
[44] V. Saranathan, C. O. Osuji, S. G. J. Mochrie, H. Noh, S. Narayanan, A. Sandy, E. R. Dufresne, and R. O. Prum, Structure, function, and self-assembly of single network gyroid $I4_132$ photonic crystals in butterfly wing scales, Proc. Natl. Acad. Sci. USA **107**, 11676 (2010).
[45] S. Vignolini, N. A. Yufa, P. S. Cunha, S. Guldin, I. Rushkin, M. Stefik, K. Hur, U. Wiesner, J. J. Baumberg, and U. Steiner, A 3D optical metamaterial made by self-assembly, Adv. Mater. **24**, OP23 (2012).
[46] J. A. Dolan, B. D. Wilts, S. Vignolini, J. J. Baumberg, U. Steiner, and T. D. Wilkinson, Optical properties of gyroid structured materials: From photonic crystals to metamaterials, Adv. Opt. Mater. **3**, 12 (2015).
[47] L. Wu, W. Zhang, and D. Zhang, Engineering gyroid-structured functional materials via templates discovered in nature and in the lab, Small **11**, 5004 (2015).
[48] J. A. Dolan, K. Korzeb, R. Dehmel, K. C. Gödel, M. Stefik, U. Wiesner, T. D. Wilkinson, J. J. Baumberg, B. D. Wilts, U. Steiner, and I. Gunkel, Controlling self-assembly in gyroid terpolymer films by solvent vapor annealing, Small **14**, 1802401 (2018).
[49] S. T. Hyde, M. O'Keeffe, and D. M. Proserpio, A short history of an elusive yet ubiquitous structure in chemistry, materials, and mathematics, Angew. Chem., Int. Ed. **47**, 7996 (2008).
[50] A. Mizuno, Y. Shuku, and K. Awaga, Recent developments in molecular spin gyroid research, Bull. Chem. Soc. Jpn. **92**, 1068 (2019).
[51] G. H. Wannier, Antiferromagnetism. The triangular Ising net, Phys. Rev. **79**, 357 (1950).
[52] *Frustrated Spin Systems*, edited by H. Diep (World Scientific, Singapore, 2004).
[53] C. Lacroix, P. Mendels, and F. Mila, *Introduction to Frustrated Magnetism* (Springer, Berlin, 2011).
[54] M.-A. Bisotti, M. Beg, W. Wang, M. Albert, D. Chernyshenko, D. Cortés-Ortuño, R. A. Pepper, M. Vousden, R. Carey, H. Fuchs, A. Johansen, G. Balaban, L. Breth, T. Kluyver, and H. Fangohr, FINMAG: Finite-element micromagnetic simulation tool, Zenodo (2018), doi:10.5281/zenodo.1216011.

[55] COMSOL AB, COMSOL MULTIPHYSICS, *version 5.3*, Stockholm, 2019.

[56] A. Hagberg, P. Swart, and D. S Chult, Exploring network structure, dynamics, and function using networkx (2008), https://www.osti.gov/biblio/960616.

[57] Y. Taguchi, Y. Oohara, H. Yoshizawa, N. Nagaosa, and Y. Tokura, Spin chirality, Berry phase, and anomalous Hall effect in a frustrated ferromagnet, Science **291**, 2573 (2001).

[58] J.-H. Park, S. Onoda, N. Nagaosa, and J. H. Han, Nematic and Chiral Order for Planar Spins on a Triangular Lattice, Phys. Rev. Lett. **101**, 167202 (2008).

[59] C. C. Wang, A. O. Adeyeye, N. Singh, Y. S. Huang, and Y. H. Wu, Magnetoresistance behavior of nanoscale antidot arrays, Phys. Rev. B **72**, 174426 (2005).

[60] S. Pignard, G. Goglio, A. Radulescu, L. Piraux, S. Dubois, A. Declémy, and J. L. Duvail, Study of the magnetization reversal in individual nickel nanowires, J. Appl. Phys. **87**, 824 (2000).

[61] D. J. Klein and M. Randić, Resistance distance, J. Math. Chem. **12**, 81 (1993).

[62] A. Fernández-Pacheco, L. Skoric, J. M. De Teresa, J. Pablo-Navarro, M. Huth, and O. V. Dobrovolskiy, Writing 3D nanomagnets using focused electron beams, Materials **13**, 3774 (2020).

[63] L. Skoric, D. Sanz-Hernández, F. Meng, C. Donnelly, S. Merino-Aceituno, and A. Fernández-Pacheco, Layer-by-layer growth of complex-shaped three-dimensional nanostructures with focused electron beams, Nano Lett. **20**, 184 (2020).

[64] G. Williams, M. Hunt, B. Boehm, A. May, M. Taverne, D. Ho, S. Giblin, D. Read, J. Rarity, R. Allenspach, and S. Ladak, Two-photon lithography for 3D magnetic nanostructure fabrication, Nano Res. **11**, 845 (2018).

[65] A. van den Berg, M. Caruel, M. Hunt, and S. Ladak, Combining two-photon lithography with laser ablation of sacrificial layers: A route to isolated 3D magnetic nanostructures, Nano Res. **16**, 1441 (2023).

[66] S. Fukami and H. Ohno, Perspective: Spintronic synapse for artificial neural network, J. Appl. Phys. **124**, 151904 (2018).